

# Gate-controlled charge transfer in Si:P double quantum dots

F E Hudson<sup>1</sup>, A J Ferguson<sup>1</sup>‡, C C Escott<sup>1</sup>, C Yang<sup>2</sup>, D N Jamieson<sup>2</sup>, R G Clark<sup>1</sup> and A S Dzurak<sup>1</sup>

<sup>1</sup> Centre for Quantum Computer Technology, Schools of Physics and Electrical Engineering, University of New South Wales, NSW 2052, Australia

<sup>2</sup> Centre for Quantum Computer Technology, School of Physics, University of Melbourne, VIC 3010, Australia

E-mail: f.hudson@unsw.edu.au

**Abstract.** We present low temperature charge sensing measurements of nanoscale phosphorus-implanted double-dots in silicon. The implanted phosphorus forms two 50 nm diameter islands with source and drain leads, which are separated from each other by undoped silicon tunnel barriers. Occupancy of the dots is controlled by surface gates and monitored using an aluminium single electron transistor which is capacitively coupled to the dots. We observe a charge stability diagram consistent with the designed many-electron double-dot system and this agrees well with capacitance modelling of the structure. We discuss the significance of these results to the realisation of smaller devices which may be used as charge or spin qubits.

‡ Present address: Microelectronics Research Centre, Cavendish Laboratory, University of Cambridge, CB3 0HE, UK

Few electron double-dot systems with controllable quantum mechanical charge or spin states are of significant interest for quantum information processing. To date, GaAs-based double quantum dots have proved the most fruitful in achieving coherent control [1, 2, 3], however, there has been recent progress in materials systems such as SiGe [4, 5, 6, 7], carbon nanotubes [8, 9] and semiconductor nanowires [10, 11, 12]. Silicon systems, for example those based on phosphorus donors in silicon (Si:P), are particularly appealing for single donor charge- and spin-based quantum information processing [13, 14, 15], promising long spin coherence times [16] as well as compatibility with existing silicon CMOS techniques. Consequently, there has been a renewed focus on the realisation of Si-based single [17] and double quantum dots [18, 20, 21, 19] in which Coulomb blockade and double-dot charging diagrams have been reported.

In this paper, we study a silicon double-dot system where the dots are defined by implantation of phosphorus donors in silicon to form nanoscale, metallicly-doped ( $n^+$ ) islands electrically isolated by regions of undoped Si. Our aim is to study Si:P double-dots of reduced dimensions and explore the possibility of realising double-dots in silicon that could operate as either charge or spin qubits. We build on recent work in which we studied transport through a single-dot with  $N \sim 600$  donors [22], charging of large double-dots containing  $N \sim 10,000$  donors [23] and experiments that used aluminium single electron transistors (SETs) to investigate the transfer of electrons between two isolated islands of P donors in silicon [24].

The devices described here have two phosphorus-doped islands separated by small gaps from ion implanted source ( $S$ ) and drain ( $D$ ) leads. These differ from the majority of other double-dot systems which use surface gates to define the dots in an underlying structure. The double-dot devices are designed to contain either  $N = 300$  or  $600$  confined electrons in each dot, with this number reduced slightly due to population of interface traps. Occupancy of the dots is manipulated by surface control gates but, due to the small dimensions of the device, the number of gates is limited to two control gates to modify the electrostatic potential of the dots. At this scale, it is difficult to include tunnel barrier control gates between each dot and the leads and so the device depends on geometrical design for appropriately high tunnel barriers. The resulting tunnel coupling is sufficiently weak to preclude direct transport measurements and so charge transfers are monitored using an aluminium SET as a charge detector.

The devices were fabricated on a high-resistivity silicon substrate with  $\rho > 5$   $\text{k}\Omega\text{cm}^{-1}$  and a weak background  $n$ -doping of less than  $10^{12}$   $\text{cm}^{-3}$ . (Figure 1(a) shows a completed device.) A 5 nm  $\text{SiO}_2$  gate oxide was thermally grown on the surface. This oxide was grown in our laboratory and has a trap density of less than  $n_{\text{trap}} = 2 \times 10^{11}$   $\text{cm}^{-2}$ , as determined from both MOSFET threshold voltages and deep level transient spectroscopy (DLTS) measurements [25].

The double-dots and source-drain leads were ion-implanted through a polymer mask defined in 150 nm-thick PMMA resist by electron beam lithography (EBL). The mask contained two 30 nm diameter apertures to define the dots and openings for source-drain leads, all separated by 100 nm gaps. For  $N = 300$  and 600 P atom dots, phosphorus was

implanted with areal doses of 4.3 and  $8.5 \times 10^{13} \text{ cm}^{-2}$  at 14 keV energy, respectively, resulting in a peak donor concentration at a depth of 20 nm below the substrate surface. Based on modelling using an industry-standard package [26], we calculate peak densities of the implanted regions to be  $n_{300} = 2.1 \times 10^{19} \text{ cm}^{-3}$  and  $n_{600} = 4.2 \times 10^{19} \text{ cm}^{-3}$ , which are an order of magnitude greater than the bulk metal-insulator transition for Si:P ( $n_{\text{MIT}} = 3.45 \times 10^{18} \text{ cm}^{-3}$ ).

Following implantation, the PMMA resist mask was removed and the implanted phosphorus regions imaged with a scanning electron microscope (SEM). Figure 1(c) shows an SEM image of an implanted device at this stage. In this image, the dark areas are due to the presence of the implanted phosphorus donors and also the damage caused by the ion implantation process. The individual dimensions of each device can be recorded and we observe that dots implanted through a 30 nm diameter aperture yield a damaged region of  $\sim 50$  nm diameter. From this we infer the diameter of the implanted dots to be  $\sim 50$  nm and the gaps between the dots and the leads to be  $\sim 80$  nm. A rapid thermal anneal (RTA) performed at 1000 °C for 5 s repaired the damage caused by the implantation process while minimising dopant diffusion [27]. The contrast between the implanted region and the undoped silicon upon SEM imaging decreases significantly after this anneal (seen in Figure 1(a)), consistent with repair of the implantation damage.

In two final EBL steps, electrostatic gates and the SET were patterned on the silicon surface. Ti/Au control gates,  $V_L$  and  $V_R$ , were fabricated using a single layer PMMA resist mask and thermal metal evaporation. The SET was defined using a bilayer polymer resist and double-angle evaporation. An in-situ oxidation was performed between the two layers to form the oxide tunnel barriers. Apertures, gates and SET were all aligned to one another with better than 50 nm precision using Ti/Pt alignment markers, chosen to withstand all processing steps, particularly the high temperature anneal. The SET is positioned centrally between the two dots which, despite being non-optimal for inter-dot transitions, still allows us to detect transfers between the dots due to a slight misalignment during fabrication.

The SET charge detection measurements were performed at the base temperature of a dilution refrigerator ( $T \sim 100$  mK) using standard low-frequency ( $f < 100$  Hz) lock-in techniques with an ac excitation voltage  $V_{\text{ac}} = 20 \mu\text{V}$ . Whilst SET sensitivity is highest in the superconducting state, the best data was obtained when a magnetic field of  $B = 0.5$  T was applied to suppress superconductivity as fewer random telegraph events were present in this state.

Devices with  $N = 600$  and 300 implanted P atoms per dot were measured. A schematic cross section of the devices is shown in Figure 1(b). The SET was biased at a point of high charge sensitivity whilst the control gates,  $V_L$  and  $V_R$ , were swept. High SET sensitivity was maintained with the SET control gate,  $V_C$ , which has negligible coupling to the dots.

A characteristic feature of a double-dot structure is a hexagonal-shaped unit cell as the two control gates are swept [28]. Each hexagonal cell represents a different charge

state and the dot occupancy is changed by one electron for adjacent cells. Source(drain) to left(right) dot ( $S(D) \leftrightarrow \text{DOT}_{L(R)}$ ) transitions are seen as horizontal(vertical) lines and triple points occur where three different charge states are degenerate. Lines connecting closest pairs of triple points denote interdot transitions, completing the hexagonal cell shape. A charging diagram mapped out from charge sensing measurements can reveal all of the charge transitions associated with the double-dot system. Note that this differs from direct transport measurements where, for example, either the hexagon cell edges or the triple points can be resolved at different tunnel barrier conductances and source-drain biases. Figure 2(a) shows SET conductance as a function of  $V_L$  and  $V_R$  for a device with 600 P donors. In Figure 2(b), a single trace of SET conductance as a function of  $V_L$  at  $V_R = 123$  mV shows the characteristic sawtooth behaviour as the charge transfers are sensed by the SET. In the charging diagram in Figure 2(a), irregular but repeating cells are observed. In Figures 3(a) and (b) we zoom in on the corners of the cells and see that each cell is an elongated hexagon shape and consistent with a double-dot structure. There is some variability across devices but several hexagon-shaped cells are observed in different areas of voltage space across different devices. This differs from previous work on devices with two isolated dots with no leads in which parallel charge transfer lines were observed as electrons were transferred between the two isolated dots [24].

We also observe a number of additional charge transfer lines in the data that are not parallel to each other or part of the hexagon cells. These are indicative of a more complicated charging structure and could be due to additional Coulomb blockade events from random disorder in the device channel, such as charge traps or unintentional P islands.

The data in Figures 3(a) and (b) show four well-defined charge states for double-dot devices with 600 and 300 P donors per dot respectively. In our geometry the SET is nominally centered between the dots and, as such, we would expect no definition between the  $(m+1, n)$  and  $(m, n+1)$  total charge states. However, in the 600 donor device, (Figure 3(a)), some definition between these two states can be observed, due to the slight misalignment of the SET towards one of the dots.

The elongated dimensions of the hexagon cells are attributed to the interdot coupling being very much smaller than the coupling between the dots and gates. The ratio of the mutual capacitance between the dots,  $C_m$ , to the total dot capacitance,  $C_{L(R)}$ , can be extracted by examining the charging diagram [28]. Firstly, the direct capacitances of the dots to their respective gates,  $C_{\text{DOT}_L-V_L}$  and  $C_{\text{DOT}_R-V_R}$ , were determined from the period of the  $S(D) \leftrightarrow \text{DOT}_{L(R)}$  charge state transitions.  $C_{\text{DOT}_L-V_L} \simeq 5.8$  aF and  $C_{\text{DOT}_R-V_R} \simeq 5.4$  aF. It is important to note that the cross-capacitances are of significant magnitude,  $C_{\text{DOT}_L-V_R}$  and  $C_{\text{DOT}_R-V_L} \sim 1-2$  aF. This is due to the reduced size of the device and hence close proximity of either gate to both dots. The triple-point separations in  $V_L$  and  $V_R$  space,  $\Delta V_L^m$  and  $\Delta V_R^m$  are marked in Figure 3(a). The ratio of interdot to total dot capacitances are calculated using the equation  $C_m/C_{L(R)} = \Delta V_{R(L)}^m (C_{\text{DOT}_{R(L)}-V_{R(L)}}/e)$ .  $C_m/C_L \simeq 0.008$  and  $C_m/C_R \simeq 0.009$ , i.e. the interdot capacitance is  $\sim 120$  times smaller than total dot capacitances. This imbalance could

be addressed if the dots were closer together or if tunnel barrier control gates were available, however, at these dimensions, it is problematic to fit so many individual gates into the device and align them accurately. Further to this, we note there is a limit on the proximity of the dots to the leads and to each other in order to maintain well isolated phosphorus regions. This limit is inherent in the implantation fabrication process [29].

In both devices, the charge induced on the SET island for the three different state transitions ( $S \leftrightarrow \text{DOT}_L$ ,  $D \leftrightarrow \text{DOT}_R$  and  $\text{DOT}_L \leftrightarrow \text{DOT}_R$ ) was found to be between  $0.02 e$  and  $0.04 e$ , with the variations being due to both misalignment of the SET and gates to the implanted dots and also to differing capacitances of the tunnel barriers across the device.

Data from the  $N = 600$  P atom device was modelled using readily available simulation programs, Crystal-TRIM, FastCap and Simon [30, 31, 32], following similar work in [33]. Crystal-TRIM is a 3D implantation simulator that predicts the implant profile and peak densities of the nanoscale dots when given the applied dose, mask geometry and target material. This package was used as it includes effects, such as channelling of dopant ions, that result from having a crystalline implantation target. Using a dose of  $4.2 \times 10^{19} \text{ cm}^{-3}$  and 30 nm implant aperture diameters with a spacing of 100 nm yields an implant profile with  $\sim 50$  nm dots separated by  $\sim 80$  nm in agreement with the SEM imaging in Figure 1(c). FastCap then uses these dimensions of the localised, metallic-density phosphorus regions and characterises the capacitive coupling strength between these regions and the surface gates. Simon, a Monte-Carlo based single electron circuit simulator, is subsequently used to model the effective single electron circuit formed by the capacitively coupled dots, leads and gates. The gate dimensions used were measured from SEM images of the device: 50 nm wide gates separated by 300 nm and a 30 nm wide SET antenna positioned between the gates. In our devices, transport measurements were precluded by weak tunnel coupling, but since Simon effectively simulates a transport measurement, a nominal value for the tunnel junction resistance that allows transport is required. We assumed a value of  $1\text{M}\Omega$  and, along with the FastCap capacitances, input this into Simon to calculate the stability diagram (shown in Figure 4(b)) for a temperature of 100mK. Table 1 compares the modelled capacitance values with the experimental values extracted from the stability diagram. We found that the capacitance and cross-capacitance values associated with dot  $\leftrightarrow$  source/drain charge state transitions fell within the limits of the experimental data error. However, there is some degree of mismatch between the model and the experimental data for the ratio of interdot to total dot capacitances,  $C_m/C_{L(R)}$ . The modelling over estimates  $C_m/C_{L(R)}$  by a factor of  $\sim 10$ . This could be due to an overestimation of the size (and hence proximity) of the implanted dots.

To extend this work further towards devices with potential as charge or spin qubits, there are a number of strategies to pursue. The implant dose could be lowered such that fewer P atoms are implanted into the dots, however, a separate implantation with a higher dose would be needed to maintain a metallic density of states in the source and drain leads. At these dimensions, alignment of the PMMA masks for each implantation

would have to be very precise so as to locate the dot centrally between the leads. A more elegant solution could be to incorporate a top gate above the dots and use it to deplete the electrons in the dot. Such a gate could also be used to control the tunnel barriers between the dots and the dots and leads, for more precise control and also to correct for any fabrication misalignments. Another alternative solution would be to use self-aligning gates made from, for example, poly-Si that would withstand the high temperature anneal. These could be designed to firstly form an implantation mask and then be used as gates which are positioned directly over the dots and tunnel barriers.

This work has shown that small implanted double-dots in silicon can be achieved and exhibit classical double-dot behaviour. Capacitance modelling showed good agreement with the measured data and device dimensions. There are various ways in which to proceed towards dots with fewer electrons where observation of excited states may lead to important coherent measurements, such as the spin states in silicon. Based on results from GaAs based double-dots, such measurements could be expected in dots with  $N < 100$  donors.

## Acknowledgments

The authors would like to thank S. E. Andresen, V. Chan and R. Brenner for helpful discussions and E. Gauja, R. P. Starrett, D. Barber, G. Tamanyan and R. Szymanski for their technical support. This work is supported by the Australian Research Council, the Australian Government and by the US National Security Agency (NSA), Advanced Research and Development Activity (ARDA) and the Army Research Office (ARO) under contract number W911NF-04-1-0290.

## References

- [1] Hayashi T, Fujisawa T, Cheong H D, Jeong Y H and Hirayama Y 2003 *Phys. Rev. Lett.* **91** 226804
- [2] Petta J R, Johnson A C, Taylor J M, Laird E A, Yacoby A, Lukin M D, Marcus C M, Hanson M P and Gossard A C 2005 *Science* **309** 2180
- [3] Koppens F H L, Buizert C, Tielrooij K J, Vink I T, Nowack K C, Meunier T, Kouwenhoven L P and Vandersypen L M K 2006 *Nature* **442** 766
- [4] Berer T, Pachinger D, Pillwein G, Muehlberger M, Lichtenberger H, Brunthaler G and Schaeffler F 2007 *Semicond. Sci. Technol.* **22** S137
- [5] Sakr M R, Yablonovitch E, Croke E T and Jiang H W 2005 *Appl. Phys. Lett.* **87** 223104
- [6] Simmons C B, Thalukulam M, Shaji N, Klein L J, Qin H, Blick R H, Savage D E, Lagally M G, Coppersmith S N and Eriksson M A 2007 *Appl. Phys. Lett.* **91** 213103
- [7] Slinker K A *et al* 2005 *New J. Phys.* **7** 246
- [8] Biercuk M J, Garaj S, Mason N, Chow J M and Marcus C M 2005 *Nano Lett.* **5** 1267
- [9] Sapmaz S, Meyer C, Beliczynski P, Jarillo-Herrero P and Kouwenhoven L P 2006 *Nano Lett.* **6** 1350
- [10] Lu W, Xiang J, Timko B P, Wu Y and Lieber C M 2005 *Proc. Natl. Acad. Sci. USA* **102** 10046
- [11] Thelander C, Mertensson T, Bjvrk M T, Ohlsson B J, Larsson M W, Wallenberg L R and Samuelson L 2003 *Appl. Phys. Lett.* **83** 2052
- [12] Zhong Z, Fang Y, Lu W and Lieber C M 2005 *Nano Lett.* **5** 1143
- [13] Kane B E 1998 *Nature* **393** 133



- [14] Hill C D, Hollenberg L C L, Fowler A G, Wellard C J, Greentree A D and Goan H S 2005 *Phys. Rev. B* **72** 045350
- [15] Hollenberg L C L, Dzurak A S, Wellard C J, Hamilton A R, Reilly D J, Milburn G J and Clark R G 2004 *Phys. Rev. B* **69** 113301
- [16] Tyryshkin A M, Lyon S A, Astashkin A V and Raitsimring A M 2003 *Phys. Rev. B* **68** 193207
- [17] Angus S J, Ferguson A J, Dzurak A S and Clark R G 2007 *Nano Lett.* **7** 2051
- [18] Gorman J, Hasko D G and Williams D A 2005 *Phys. Rev. Lett.* **95** 090502
- [19] Shin S J, Lee J J, Chung R S, Kim M S, Park E S, Choi J B, Kim N S, Park K H, Lee S D, Kim N and Kim J H 2007 *Appl. Phys. Lett.* **91** 053114
- [20] Hofheinz M, Jehl X, Sanquer M, Molas G, Vinet M and Deleonibus S 2006 *Appl. Phys. Lett.* **89** 143504
- [21] Fujiwara A, Inokawa H, Yamazaki K, Namatsu H, Takahashi Y, Zimmerman N M and Martin S B 2006 *Appl. Phys. Lett.* **88** 053121
- [22] Hudson F E, Ferguson A J, Yang C, Jamieson D N, Dzurak A S and Clark R G 2006 *Microelectron. Eng.* **83** 1809
- [23] Chan V C, Buehler T M, Ferguson A J, McCamey D R, Reilly D J, Dzurak A S, Clark R G, Yang C and Jamieson D N 2006 *J. Appl. Phys.* **100** 106104
- [24] Buehler T M *et al* 2006 *Appl. Phys. Lett.* **88** 192101
- [25] McCamey D R, Francis M, McCallum J C, Hamilton A R, Greentree A D and Clark R G 2005 *Semicond. Sci. Technol.* **20** 363
- [26] Ziegler J F, Biersack J P and Littmark U 1985 *SRIM – The Stopping and Range of Ions in Solids* (New York: Pergamon Press)
- [27] Oehrlein G S, Cohen S A and Sedgwick T O 1984 *Appl. Phys. Lett.* **45** 417
- [28] van der Wiel W G, Franceschi S D, Elzerman J M, Fujisawa T, Tarucha S and Kouwenhoven L P 2003 *Rev. Mod. Phys.* **75** 1
- [29] Jamieson D N *et al* 2006 *Nucl. Instrum. Methods Phys. Res. B* **249** 221
- [30] Posselt M, Schmidt B, Feudel T and Strecker N 2000 *Mater. Sci. Eng., B* **71** 128
- [31] Nabors K and White J 1991 *IEEE Trans. Comput.-Aided Des.* **10** 1447
- [32] Wasshuber C, Kosina H and Selberherr S 1997 *IEEE Trans. Comput.-Aided Des.* **16** 937
- [33] Escott C C, Hudson F E, Chan V C, Petersson K D, Clark R G and Dzurak A S 2007 *Nanotechnology* **18** 235401

	Experimental	Modelling
$C_{\text{DOT}_L-V_L}$ (aF)	$5.8 \pm 1.6$	4.2
$C_{\text{DOT}_R-V_R}$ (aF)	$5.4 \pm 1.6$	3.8
$C_{\text{DOT}_L-V_R}$ (aF)	1-2	1.8
$C_{\text{DOT}_R-V_L}$ (aF)	1-2	1.7
$C_m/C_L$	0.008	0.09
$C_m/C_R$	0.009	0.13

**Table 1.** Measured and calculated capacitance and cross-capacitance values for dot to source/drain transitions and ratios of interdot to total dot capacitances.

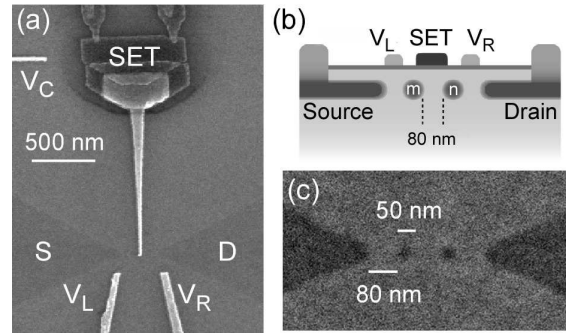


**Figure 1.** (a) SEM image of a Si:P double-dot device with two surface control gates and SET. (b) Schematic cross-section of implanted device. (c) SEM image of double-dots and leads after implantation but before annealing. Regions of dark contrast indicate implanted phosphorus and pre-anneal damage in the silicon.



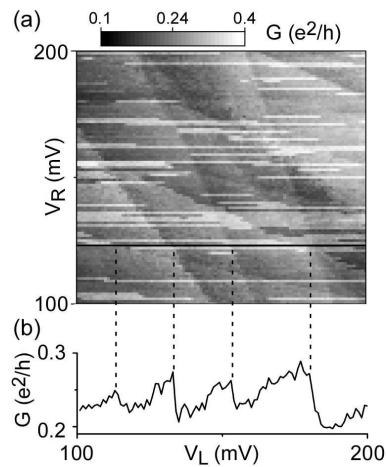


**Figure 2.** (a) Conductance of SET showing charge transfer events as a function of  $V_L$  and  $V_R$  in an  $N = 600$  P atom device. Elements of an irregular hexagonal charging diagram are observed. (b) Single trace of SET conductance plotted as a function of  $V_L$  at  $V_R = 123$  mV. A sawtooth signature is seen as the SET detects each charge transfer.

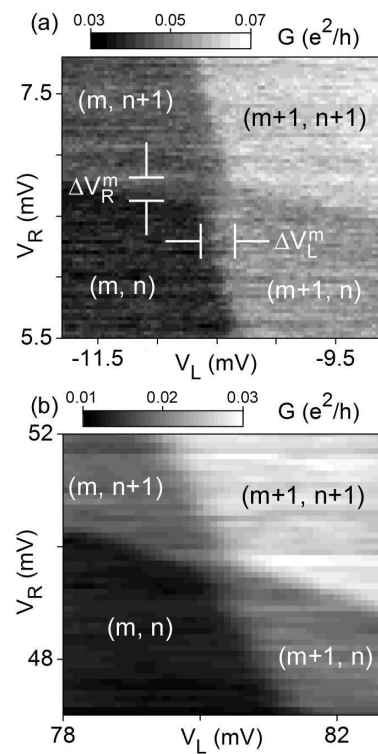


**Figure 3.** (a) and (b) SET conductance for devices with  $N = 600$  and  $300$  P atoms per dot (respectively) showing hexagonal cells in the charging diagram. Relative electron population of the dots within the four charge states are shown.

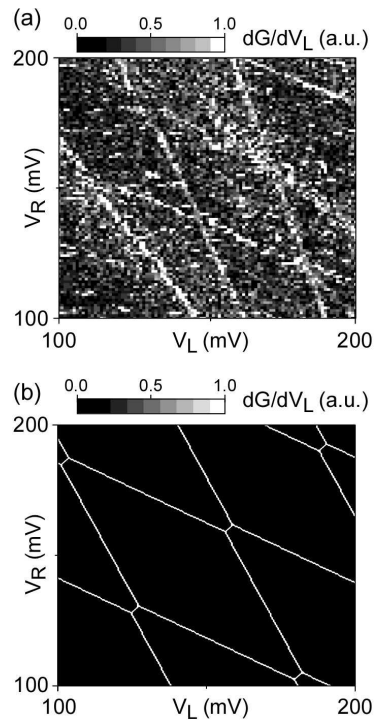


**Figure 4.** (a) Differential conductance of SET as a function of  $V_L$  and  $V_R$  in the  $N = 600$  P atom device. (b) Numerical modelling of the device in (a).